Interpolating Spherical Harmonics for Computing Antenna Patterns

J. Rockway
J. Meloling
J. C. Allen

SSC Pacific

Interpolating Spherical Harmonics for Computing Antenna Patterns

J. Rockway
J. Meloling
J. Allen

SSC Pacific
San Diego, CA 92152-5001

ADMINISTRATIVE INFORMATION

SB

EXECUTIVE SUMMARY

The classic orthogonal expansion of antenna patterns by spherical harmonics is finding new applications in computational electromagnetics, antenna design, and wireless systems. For example, recent research uses spherical harmonics to decouple the multiple antennas in a multiple-input multiple output (MIMO) radio system from the propagation medium. This approach reveals "that channel capacity is dependent on the number and distribution of the spherical modes." Consequently, the spherical harmonics force an end-to-end approach to MIMO systems designs—adaptively excite selected spherical modes to maximize channel capacity.

This report reviews spherical harmonic expansions to compute wideband antenna patterns. Some "antenna" patterns, such as the far-field of a ship, require lots of computer time per each frequency. Consequently, computing such a pattern across a wide frequency band at each frequency is prohibitive. Spherical harmonics offer an alternative—compute the pattern over a coarse sampling across the frequency band, interpolate the spherical harmonics, and use these harmonics to recover the pattern at a fine frequency sampling with small CPU. This report develops an adaptive spline interpolation algorithm with error control. The development used antennas with smooth analytic patterns for verification. Further developments must test this algorithm on a suite of tactical antenna patterns.

Contents

List of Figures

List of Tables

1 Spherical Harmonics and Antenna Patterns

Spherical harmonic expansions can speed antenna and electromagnetic (EM) computations. The spherical harmonics $\{Y_n^m\}$ are an orthonormal basis for the square-integrable functions on the sphere [1, page 572]: if $g \in L^2(\mathbb{S})$,

$$g(\theta, \phi) = \sum_{n=0}^{\infty} \sum_{m=-n}^{n} g_n^m Y_n^m(\theta, \phi).$$

One natural application for spherical harmonic expansions is in the ray-tracing codes that require the near-field antenna patterns to be integrated with the ray tracings. Figure 1 shows a logarithmic antenna and its patterns at 3 and 6 GHz [2].
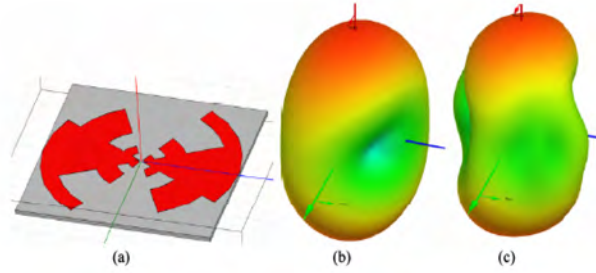
Figure 1: (a) logarithmic antenna (b) pattern at 3 GHz (c) pattern at 6 GHz [2, Figure 4].

If this antenna operates in the indoor environment of Figure 2(a) and the wideband channel response in Figure 2(b) is to be computed, each ray that penetrates the transmitter and receiver's patterns must be weighted with the pattern's amplitude and phase over a dense sampling of the frequency band.

The computation of all the patterns over a wide and densely sampled frequency band is considerable and the standard (f, θ, ϕ)-table lookup slows the ray-trace computation. The spherical harmonic expansion takes the form [10]

$$g(\theta, \phi; f) = \sum_{n=0}^{\infty} \sum_{m=-n}^{n} g_n^m(f) Y_n^m(\theta, \phi).$$

Each coefficient $g_n^m(f)$ is a function of frequency that is decoupled from the angles. More practically, the compact antenna need only a few spherical
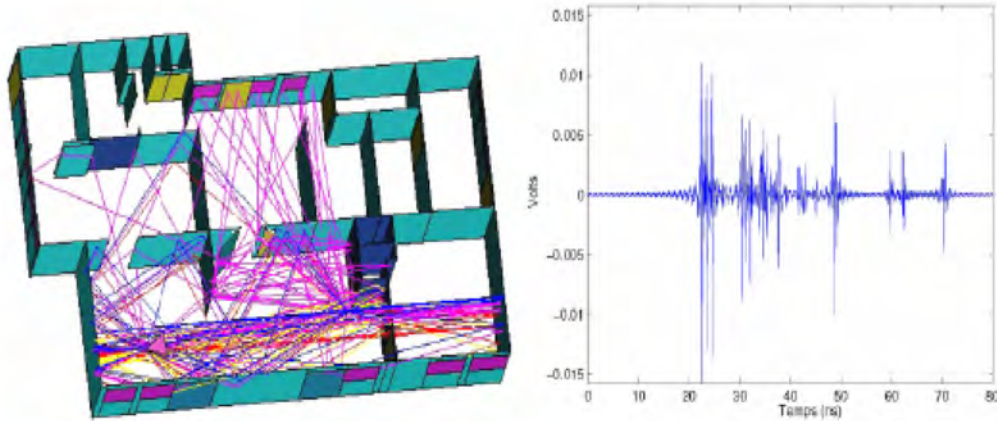
Figure 2: (a) indoor rays (b) time-domain channel response; [2, Figure 1].

coefficients to approximate an antenna pattern [2]. Because the spherical harmonics $Y_n^m(\theta, \phi)$ admit fast computations, spherical expansion avoids the slower table-lookups. More importantly, the coefficients $g_n^m(f)$ are smooth functions of frequency. If an antenna pattern requires a day to compute per frequency, computing a dense sampling of the patterns across the frequency band is impossible. However, if the patterns can be interpolated with controlled error using only a few samples, any sampling density of the patterns across the frequency band is possible.

This report offers a simple adaptive spline interpolation (ASI) algorithm to benchmark more sophisticated pattern approximation methods. Section 2 sets out two antenna patterns to be tested in the spline algorithm. Section 3 reviews the spherical harmonic functions $Y_n^m(\theta, \phi)$ and their expansions. Section 4 uses one of the antenna patterns to develop the ASI algorithm and the error bounds. Section 5 tests the ASI algorithm on the more difficult antenna pattern. Section 6 discusses applications of spherical harmonics with an emphasis on MIMO wireless that include polarizations.

2

2   Short-Wire Antennas

Two short-wire antenna are reviewed to set the notation and motivate the spherical harmonic approach. Figure 3 illustrates spherical coordinates around a short antenna carrying a $\widehat{\mathbf{z}}$-directed current in free space:
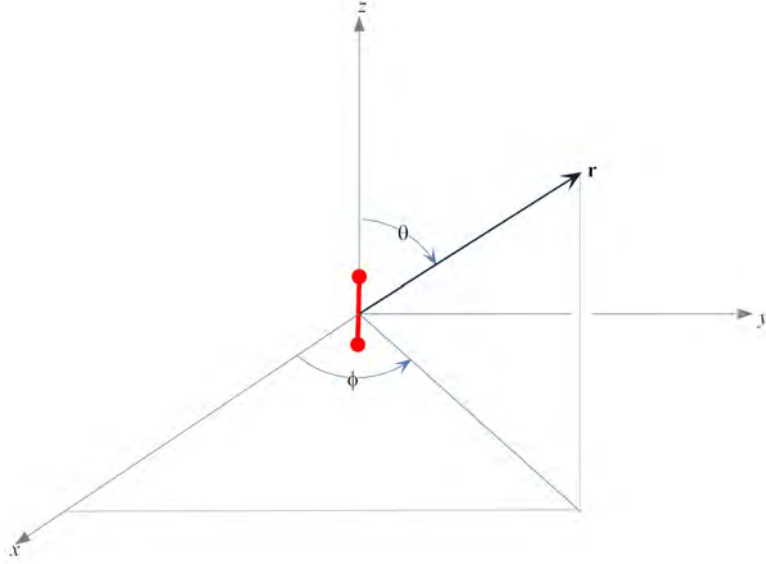
Figure 3: Spherical coordinates.

The magnetic vector potential is [4, Eq. 13-47]:

$$\mathbf{A}(\mathbf{r};t) = \frac{\mu}{4\pi} \int_{-h/2}^{h/2} \frac{\mathbf{J}(z';t - \|\mathbf{r} - \mathbf{r}(z')\|c^{-1})}{\|\mathbf{r} - \mathbf{r}(z')\|} dz'; \quad \mathbf{r}(z') = \begin{bmatrix} 0 \\ 0 \\ z' \end{bmatrix}. \quad (1)$$

When the wire carries a uniform current I_0 amps at frequency f,

$$\mathbf{J}(z';t) = \widehat{\mathbf{z}} I_0 \exp(+j 2\pi f t),$$

the magnetic vector potential is

$$
\begin{aligned}
\mathbf{A}(\mathbf{r};t) &= \widehat{\mathbf{z}}I_0\frac{\mu}{4\pi}\int_{-h/2}^{h/2}\frac{\exp(+j2\pi f\{t-\|\mathbf{r}-\mathbf{r}(z')\|c^{-1}\})}{\|\mathbf{r}-\mathbf{r}(z')\|}dz' \\
&= \widehat{\mathbf{z}}I_0\frac{\mu}{4\pi}e^{+j2\pi ft}\int_{-h/2}^{h/2}\frac{\exp(-j2\pi fc^{-1}\|\mathbf{r}-\mathbf{r}(z')\|\})}{\|\mathbf{r}-\mathbf{r}(z')\|}dz' \\
&= \widehat{\mathbf{z}}I_0\frac{\mu}{4\pi}e^{+j2\pi ft}\int_{-h/2}^{h/2}\frac{\exp(-jk\|\mathbf{r}-\mathbf{r}(z')\|\})}{\|\mathbf{r}-\mathbf{r}(z')\|}dz',
\end{aligned}
$$

where k denotes the *wavenumber* with wavelength λ:

$$
k = \frac{2\pi f}{c} = \frac{2\pi}{\lambda}.
$$

With a slight abuse of notation, the Fourier component of the magnetic vector potential—in cylindrical coordinates—admits the representation

$$
\mathbf{A}(r_{\mathrm{cyn}}, z, \phi; f) = \widehat{\mathbf{z}}I_0\frac{\mu}{4\pi}\int_{-h/2}^{h/2}\frac{\exp\left(-jk\sqrt{r_{\mathrm{cyn}}^2+(z-z')^2}\right)}{\sqrt{r_{\mathrm{cyn}}^2+(z-z')^2}}dz'. \qquad (2)
$$

The field is rotationally constant around the z-axis and symmetric with respect to z. Figures 4, 5, 6, and 7 illustrate the magnetic vector potential in range and elevation as a function of increasing wire length. For this short-wire antenna, these plots show that the number of lobes in the pattern is approximately the ratio of the wire's length h to the wavelength λ.
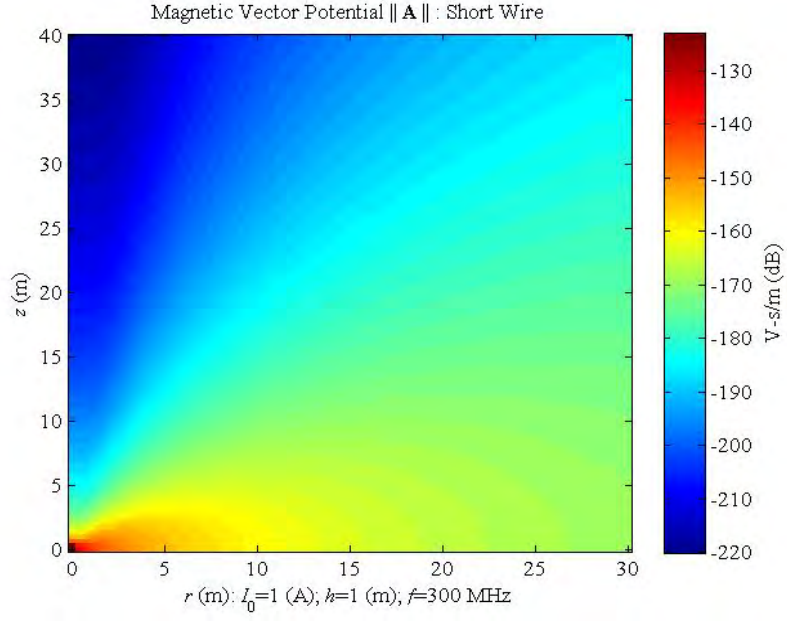
Figure 4: r-z slice of the magnetic vector potential $(h = \lambda)$.
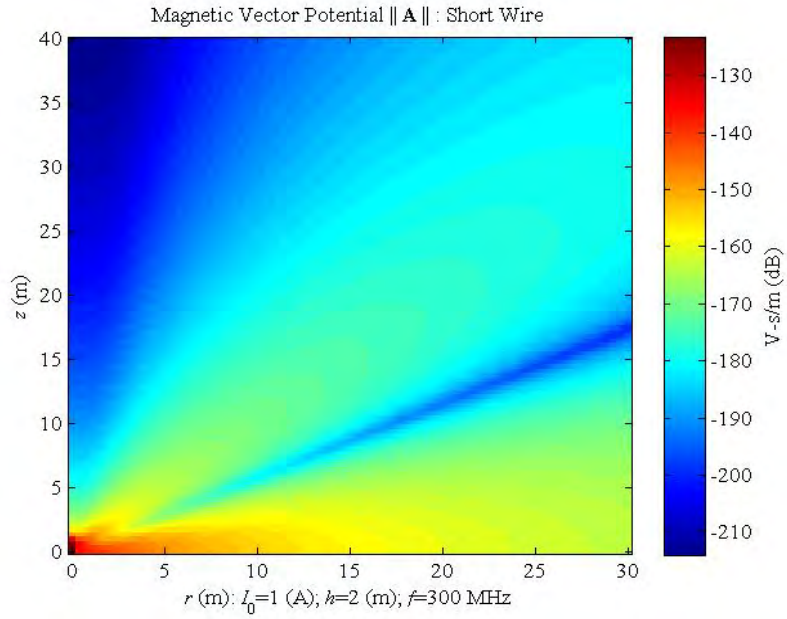
Figure 5: r-z slice of the magnetic vector potential $(h = 2\lambda)$.

5
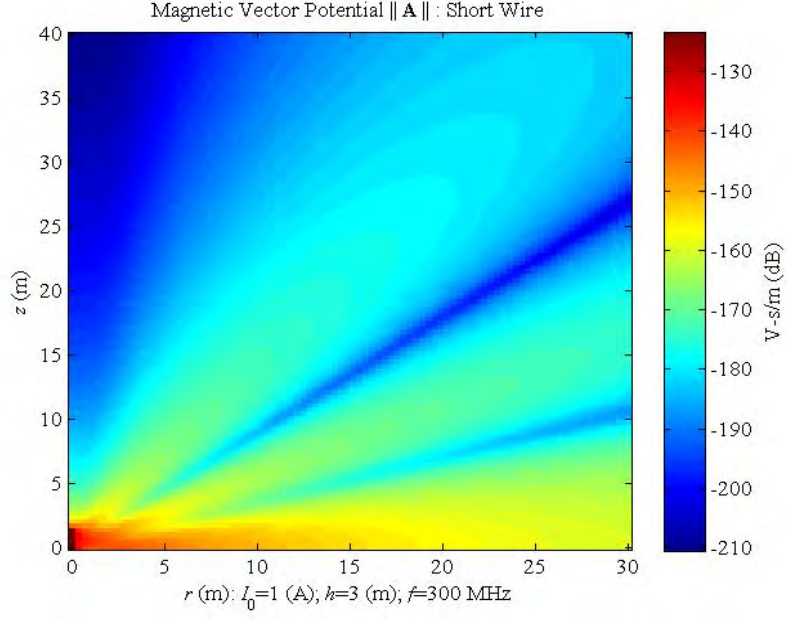
Figure 6: r-z slice of the magnetic vector potential ($h = 3\lambda$).
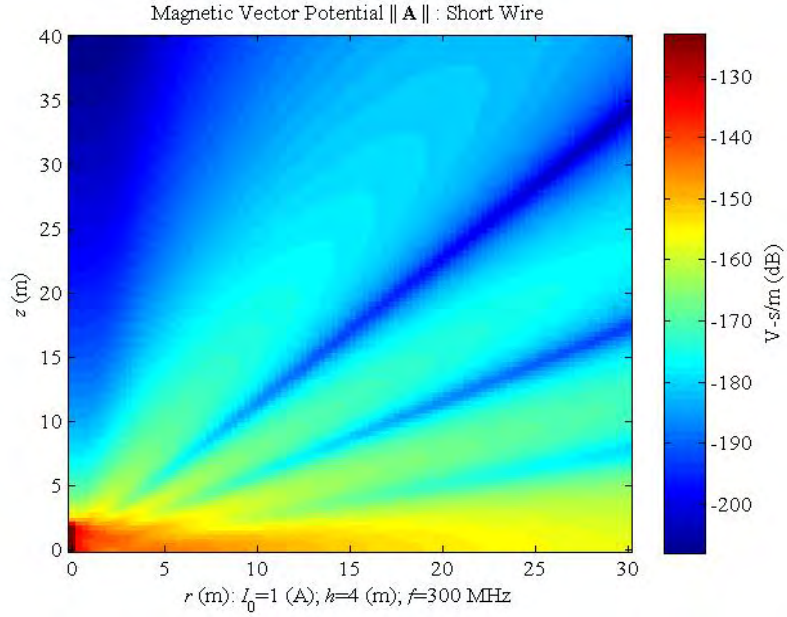
Figure 7: r-z slice of the magnetic vector potential ($h = 4\lambda$).

When the current has the more physically-plausible distribution [7, Eq. 2-124]

$$\mathbf{J}(z'; k) = \widehat{\mathbf{z}} I_m \sin(k(h/2 - |z'|)),$$

the magnetic vector potential in the radiation zone $(r \gg h)$ admits the approximation [7, page 82]

$$\mathbf{A}(r, \theta, \phi; k) \approx \widehat{\mathbf{z}} \, I_m e^{-jkr} \frac{\mu}{2\pi r} \frac{\cos(kh\cos(\theta)) - \cos(kh/2)}{k\sin(\theta)^2}. \tag{3}$$

The field is rotationally constant around the z-axis and symmetric with respect to z. Figures 8, 9, 10, and 11 illustrate the magnetic vector potential in range and elevation as a function of increasing wire length.
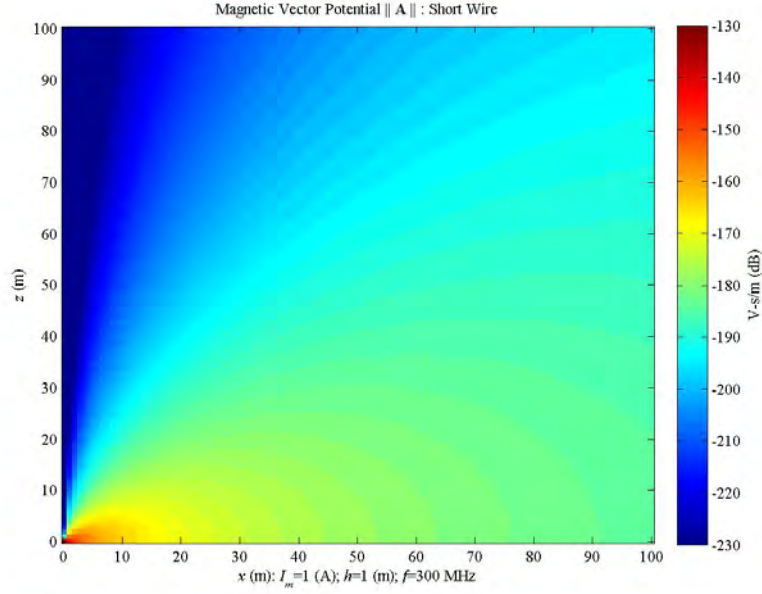
Figure 8: x-z slice of the magnetic vector potential with sinusoidal current $(h = 1$ m$)$.
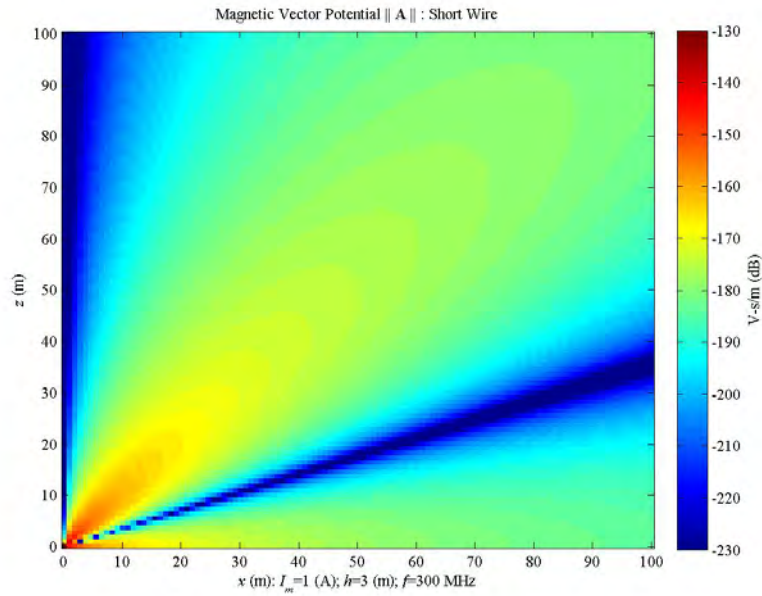
Figure 9: x-z slice of the magnetic vector potential with sinusoidal current $(h = 3$ m$)$.
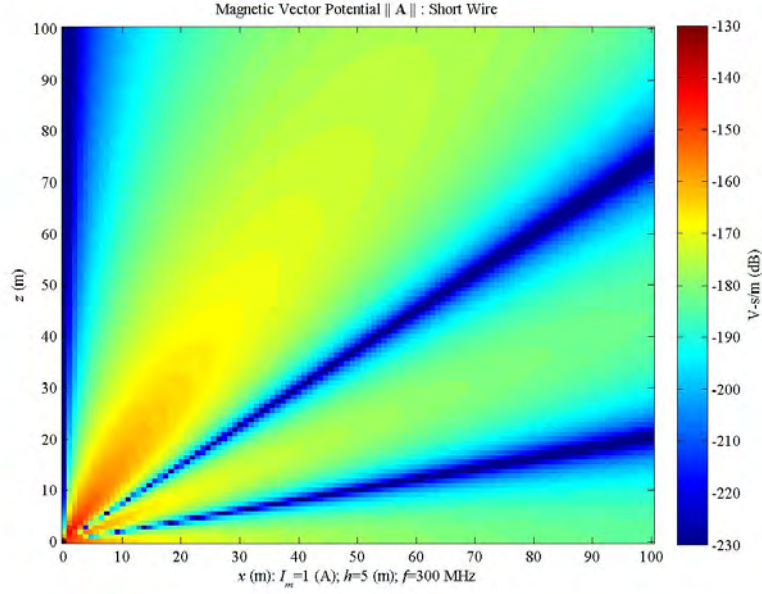
Figure 10: *x-z* slice of the magnetic vector potential with sinusoidal current ($h = 5$ m).
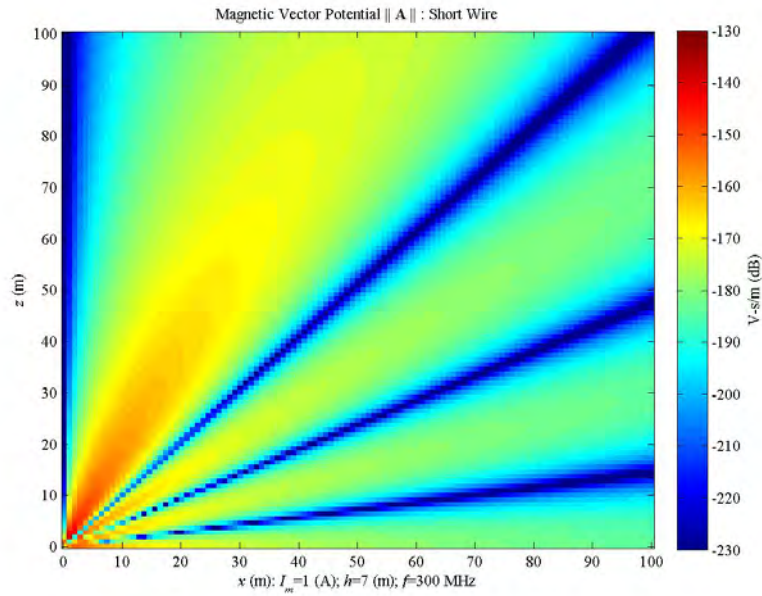
Figure 11: *x-z* slice of the magnetic vector potential with sinusoidal current ($h = 7$ m).

9

3   Spherical Harmonic Expansions

The spherical harmonics are computed for a short-wire antenna to get a baseline example for the spline interpolants. The spherical harmonics $\{Y_n^m\}$ are the functions defined on the sphere [1, Eq 12.149]

$$Y_n^m(\theta, \phi) = (-1)^m \sqrt{\frac{2n+1}{4\pi} \frac{(n-m)!}{(n+m)!}} P_n^m(\cos(\theta)) e^{jm\phi}, \qquad (4)$$

where the P_n^m's are the *associated Legendre functions*. Figure 12 plots the *normalized* associated Legendre functions [1, Eq 12.148]

$$\mathcal{P}_n^m(\cos(\theta)) = \sqrt{\frac{2n+1}{2} \frac{(n-m)!}{(n+m)!}} P_n^m(\cos(\theta))$$

for $n = 4$ and $m = 0, 1, 2, 3, 4$.
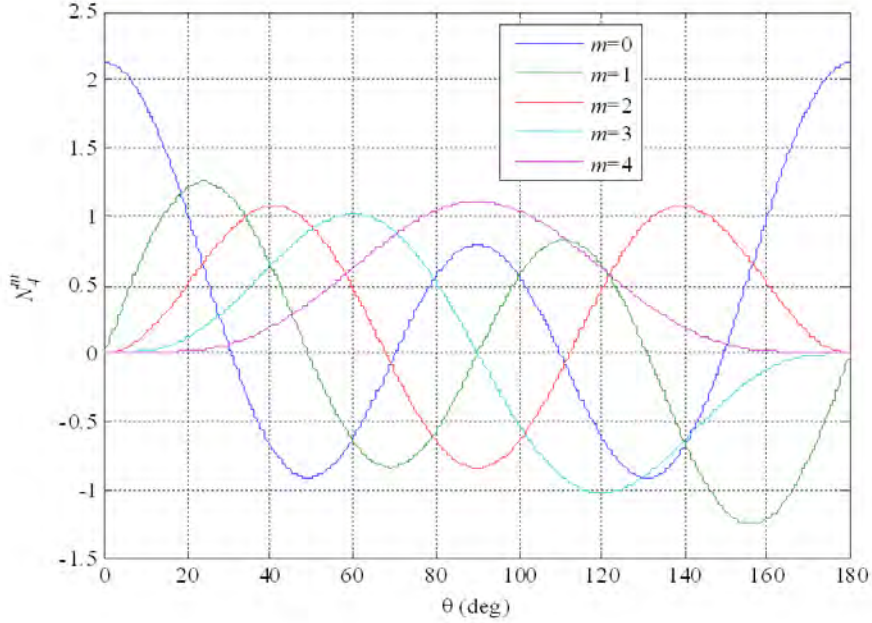
Figure 12: r-z slice of the magnetic vector potential.

Although $\mathcal{P}_n^m$'s are orthonormal with respect to the inner product for

10

fixed m [1, Eq. 12.107]

$$\langle \mathcal{P}_n^m, \mathcal{P}_{n'}^m \rangle = \int_0^\pi \mathcal{P}_n^m(\cos(\theta))\mathcal{P}_{n'}^m(\cos(\theta)) \, \sin(\theta)d\theta = \delta_{n,n'},$$

it is the complex sinusoid $\exp(jm\phi)$ that forces orthogonality over both indices [1, Eq. 12.150]:

$$\langle Y_n^m, Y_{n'}^{m'} \rangle = \int_{\theta=0}^\pi \int_{\phi=0}^{2\pi} Y_n^m(\theta, \phi)Y_{n'}^{m'}(\theta, \phi) \sin(\theta)d\theta d\phi = \delta_{m,m'}\delta_{n,n'}.$$

The spherical harmonics $\{Y_n^m\}$ are an orthonormal basis for the square-integrable functions on the sphere [1, page 572]: if $g \in L^2(\mathbb{S})$

$$g(\theta, \phi) = \sum_{n=0}^\infty \sum_{m=-n}^n g_n^m Y_n^m(\theta, \phi).$$

Example 1 (Sinusoidal Current) *Let $g(f) \in L^2(\mathbb{S})$ be the collection of patterns*

$$g(\theta, \phi; f) = \frac{\cos(kh\cos(\theta)) - \cos(kh/2)}{k\sin(\theta)^2}; \quad (2\pi f = kc)$$

extracted from Equation 3 that are indexed by frequency f. All the spherical harmonics vanish for $m \neq 0$ because this pattern is constant in ϕ:

$$g(\theta, \phi; f) = \sum_{n=0}^\infty g_n^0(f)Y_n^0(\theta, \phi).$$

Because this pattern symmetric in z, All the spherical harmonics vanish for n odd because this pattern symmetric in z:

$$g(\theta, \phi; f) = \sum_{n=0}^\infty g_{2n}^0(f)Y_{2n}^0(\theta, \phi).$$

Figure 13 plots estimate of these coefficients for the short-wire antenna with 1-meter length and the frequencies $f_0 = 300 \times \{1, 3, 5, 7\}$ MHz (The lines are added for clarity). The plot shows that the coefficients roll off rapidly with increasing index. The plot also shows that the higher frequencies take longer to roll off in concordance with the lobing seen in Figures 8, 9, 10, and 11.

Figure 14 plots the first few Legendre coefficients as functions of frequency. These coefficients plot like the Bessel functions with the "DC" coefficient $g_0^0(f)$ decreasing as the frequency increases.
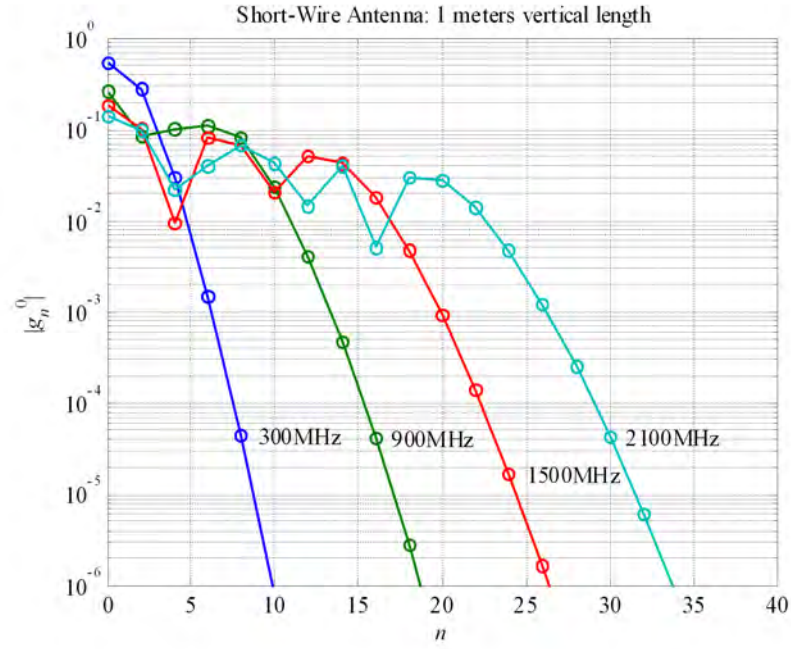
Figure 13: Legendre coefficients for selected frequencies.
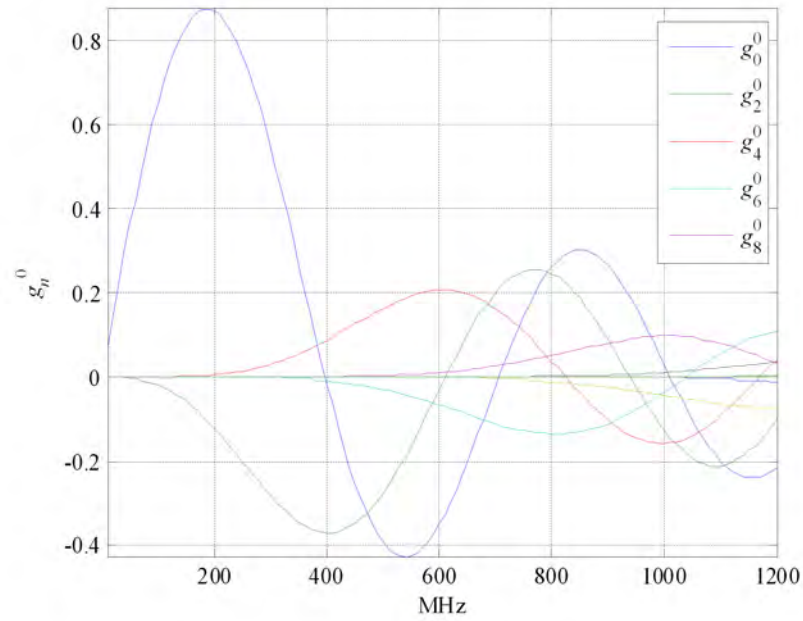
Figure 14: Selected Legendre coefficients as functions of frequency.

12

Example 2 offers two guides for sparse interpolation:

- If increasing frequency always forces the most detail in the pattern, expanding at the highest frequency shows the number of spherical coefficients to retain.

- If the spherical coefficients always show this smooth sinusoidal function of frequency, spline interpolation will be sufficient for interpolation.

The next section develops an adaptive spline interpolation using this example.

4 Adaptive Spline Interpolation (ASI)

The problem of adaptive interpolation for pattern synthesis assumes:

- computing a pattern $g(\theta, \phi; f)$ is costly,

- the spherical coefficients $\{g_n^m(f)\}$ vary smoothly as functions of frequency,

- the number of spherical coefficients to retain has been determined from the highest frequency.

Under these assumptions, the spherical coefficients $\{g_n^m\}$ can be approximated by high-accuracy splines using relatively few frequency samples. This section shows that a sequence of splines can rapidly approximate the spherical coefficients $\{g_n^m(f)\}$ with computable error bounds. A spline algorithm is developed using the short-wire antenna of Example 1. The algorithm is based on the rapid convergence of the splines to a smooth function.

Theorem 1 (Spline Convergence) *[11, Theorem 2.4.3.3]*
Let $g \in C^4([f_{\min}, f_{\max}])$. Let Δ denote a partition

$$\Delta = \{f_{\min} = f_0 < \cdots < f_{N_F} = f_{\max}\}$$

with mesh size and deviation from uniformity measured as

$$\|\Delta\|_\infty = \max\{|f_n - f_{n-1}| : n = 1, \ldots, N_F\},$$

$$\|\Delta\|_{-\infty} = \min\{|f_n - f_{n-1}| : n_f = 1, \ldots, N_F\}.$$

If g_Δ is the spline that interpolates g on Δ and satisfies $g'_\Delta(f) = g'(f)$ at $f = f_{\min}, f_{\max}$, then there exists constants $C_k \leq 2$ that do not depend on the partition such that

$$\|g_\Delta^{(k)} - g^{(k)}\|_\infty \leq C_k \|g^{(4)}\|_\infty \frac{\|\Delta\|_\infty^{5-k}}{\|\Delta\|_{-\infty}}, \quad k = 0, 1, 2, 3.$$

14

If the partitions are uniform, the splines converge as

$$\|g_\Delta - g\|_\infty \le C_0 \|g^{(4)}\|_\infty \|\Delta\|_\infty^4.$$

If g_{N_F} denotes the spline computed from the uniform partition of $N_F + 1$ frequency points, the splines converge as $\mathcal{O}[N_F^{-4}]$:

$$\|g_N - g\|_\infty \le C_0 \|g^{(4)}\|_\infty \left(\frac{f_{\max} - f_{\min}}{N_F}\right)^4 =: \frac{C_F}{N_F^4}. \tag{5}$$

That is, doubling the number of sample points reduces the error by a factor of 16 and reuses the previously computed sample points. This spline algorithm is developed using the pattern $g(\theta, \phi; f)$ obtained from the short-wire antenna of Example 1. This pattern has the expansion

$$g(\theta, \phi; f) = \frac{\cos(kh\cos(\theta)) - \cos(kh/2)}{k\sin(\theta)^2} = \sum_{n=0}^{\infty} g_{2n}^0(f) Y_{2n}^0(\theta, \phi).$$

Figures 15, 16, and 17 show the splines computed from 5, 9, and 17 equally spaced frequency samples for a 1-meter wire ($h = 1$). The spherical coefficients $\{g_{2n}^0(f)\}$ are the solid lines. The dashed lines are the splines. The circles mark the interpolation points that are the only information available to the analyst. The splines show rapid convergence to the unknown spherical coefficients $\{g_{2n}^0(f)\}$. Theorem 1 allows error estimates to be extracted from this sequence of splines.
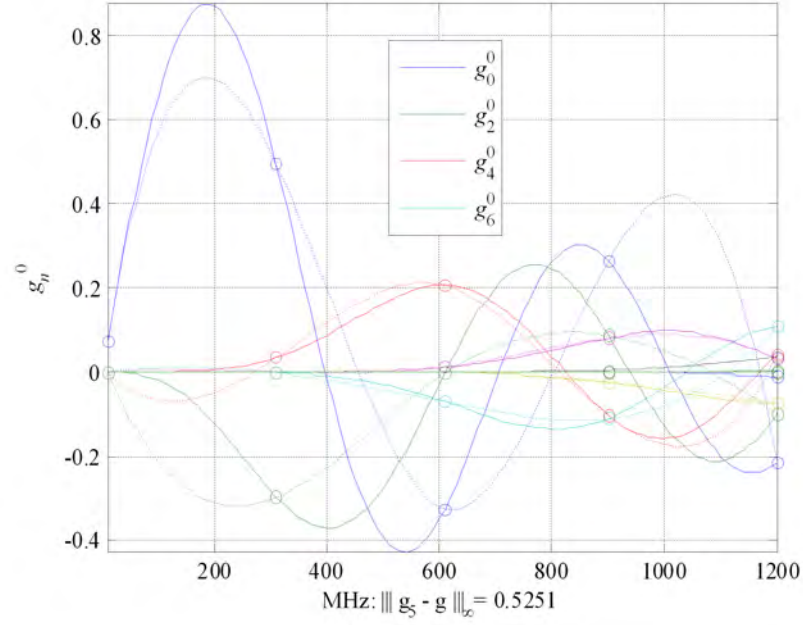
Figure 15: Legendre coefficients and five-point splines.
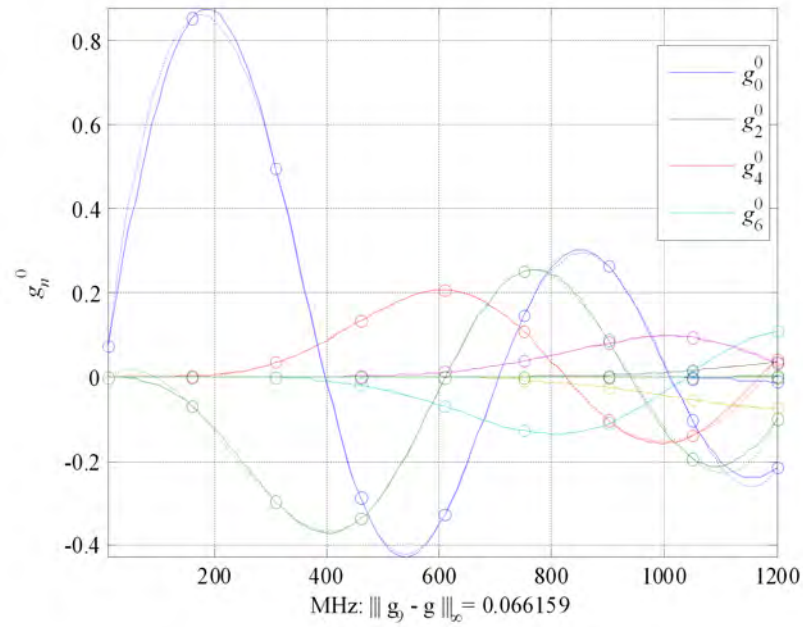
Figure 16: Legendre coefficients and nine-point splines.

16
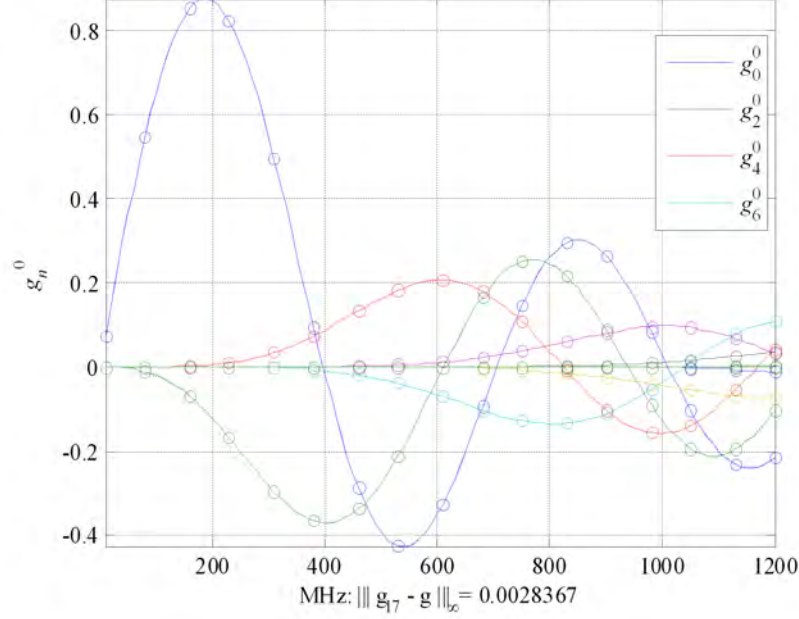
Figure 17: Legendre coefficients and 17-point splines.

There is the possibility of estimating the error $\|g - g_{N_F}\|_\infty$ even though the function g is unknown. Table 1 compares these unknown errors $\|g - g_{N_F}\|_\infty$ to the computable estimates $\|g_{N_F} - g_{2N_F}\|_\infty$. The latter is a strong predictor of the unknown error. The triple bar is the sup-norm error over all the coefficients:

$$\|\|g - g_{N_F}\|\|_\infty := \max\{\|g_n^m - g_n^m{}_{N_f}\|_\infty : n = 0, 1, \ldots, N; -n \leq m \leq n\}.$$

The remainder of this section develops two error estimates and incorporates these estimate into the adaptive spline algorithm.

The first error estimate is obtained from the observation that "doubling the sample points reduces the error by a factor of 16." This approximation

$$\|g - g_{2N_F}\|_\infty \approx \frac{1}{16}\|g - g_{N_F}\|_\infty. =$$

and the triangle inequality

$$\begin{aligned} \|g - g_{N_F}\|_\infty &\leq \|g - g_{2N_F}\|_\infty + \|g_{2N_F} - g_{N_F}\|_\infty \\ &\approx \frac{1}{16}\|g - g_{N_F}\|_\infty + \|g_{2N_F} - g_{N_F}\|_\infty \end{aligned}$$

17

Table 1: Spline convergence.

N_F	$\|\|g - g_{N_F}\|\|_\infty$	$\|\|g_{2N_F} - g_{N_F}\|\|_\infty$	$\frac{16}{15}\|g_{2N_F} - g_{N_F}\|_\infty$	C_F
4	0.5251	—	0.5683947	—
8	0.066159	0.53287	0.0696491	129
16	0.0028367	0.065296	0.0029790	252
32	0.00012164	0.0027928	0.0001219	173
64	0.0000098425	0.00011428	—	113

yield the "16/15" estimate of the error listed in Table 1:

$$\|g - g_{N_F}\|_\infty \approx \frac{16}{15}\|g_{2N_F} - g_{N_F}\|_\infty. \tag{6}$$

The second error estimate uses Inequality 5

$$\|g - g_{N_F}\|_\infty \leq \frac{C_F}{N^4}$$

to estimate C_F from the spline over the finer mesh:

$$\|g_{N_F} - g_{2N_F}\|_\infty \leq \|g_{N_F} - g\|_\infty + \|g - g_{2N_F}\|_\infty \leq \frac{C_F}{N_F^4} + \frac{C_F}{16N_F^4}.$$

This inequality produces a *lower bound* for C_F listed in Table 1:

$$\frac{16N_F^4}{17}\|g_{N_F} - g_{2N_F}\|_\infty \leq C_F. \tag{7}$$

18

Figure 18 applies these estimates to the data in Table 1. The unknown error $\|g - g_{N_F}\|_\infty$ is plotted as the blue line marked with circles. The "16/15" estimator of Equation 6 is plotted as the dashed red line. This estimator closely tracks this error but cannot predict the error for arbitrary N_F. The C_F/N_F^4 estimator is plotted as the dotted green line using $C_F = 252$ obtained from $N_F = 16$. This estimate predicts that $N_F = 64$ is necessary to push the error below 10^{-4}. As the number frequency points double, the analyst can monitor the running error and update the C_F/N_F^4 estimate.
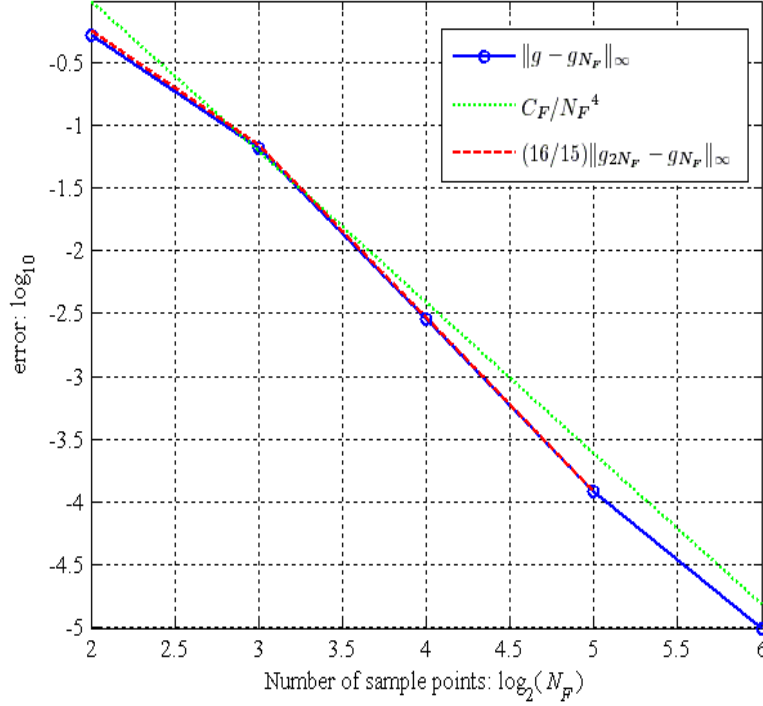

Figure 18: Spline convergence for Example 2.

This process of doubling the number of frequency samples and monitoring the convergence of the splines is summarized in the following algorithm. At each stage, the running error estimate is computed by the "16/15" estimate ϵ_1. The predicted number of sample points is computed from the asymptotic bound ϵ_2 and reported for CPU decisions. When the running estimate beats the user's error bound, the last computed spline is reported and its error bound is estimated using the asymptotic bound ϵ_2.

Algorithm 1 (Frequency Doubling)

1. *Estimate the number of Legendre coefficients to compute.*

2. *Set the error ϵ.*

3. *Set $N_F = 4$ and compute g_4.*

    (a) *compute g_{2N_F}.*

    (b) *estimate $\epsilon_1(N_F) := (16/15) \times \|g_{2N_F} - g_{N_F}\|_\infty$.*

    (c) *compute C_{N_F} from Equation 7.*

    (d) *estimate $\epsilon_2(N_F) := \max\{C_{N_F}\}/N_F^{-4}$ and report the estimated sampling necessary for $\epsilon_2(N_F) \le \epsilon$.*

    (e) *break if $\epsilon_1(N_F) \le \epsilon$ or set $N_F := 2N_F$ and loop back to (a).*

4. *Report the approximation as the last spline g_{N_F}.*

5. *Estimate the error as $\epsilon_2(N_F)$.*

20

5   Testing the ASI Algorithm

When the wire carries a uniform current I_0 amps at frequency f,

$$\mathbf{J}(z'; t) = \widehat{\mathbf{z}} I_0 \exp(+j 2\pi f t),$$

the magnetic vector potential is computed by Equation 2 and plotted in Figures 4, 5, 6, and 7. The magnetic vector potential in the radiation zone $(r \gg h)$ at the frequency of the current [7, Eq. 2-122] is

$$
\begin{aligned}
A_z(r, \theta, \phi; f) &\approx \frac{e^{jkr}}{4\pi r} \int_{-h/2}^{h/2} J(z') e^{jkz' \cos(\theta)} \, dz' \\
&= I_0 \frac{e^{jkr}}{4\pi r} \int_{-h/2}^{h/2} e^{jkz' \cos(\theta)} \, dz' \\
&= I_0 \frac{e^{jkr}}{4\pi r} \int_{-h/2}^{h/2} \cos(kz' \cos(\theta)) \, dz'.
\end{aligned}
$$

For comparison with the sinusoidal current, define the uniform current pattern as

$$g_U(\theta, \phi; f) := \int_{-1/2}^{1/2} \cos(kz' \cos(\theta)) \, dz'.$$

This section applies the Frequency-Doubling Algorithm to estimate the spherical coefficients $\{g_n^m\}$ of the expansion

$$g_U(\theta, \phi; f) = \sum_{n=0}^{\infty} \sum_{m=-n}^{n} g_{2n}^m(f) Y_{2n}^m(\theta, \phi).$$

Example 2 (Uniform Current) *Because this pattern is constant in ϕ and symmetric in z,*

$$g_U(\theta, \phi; f) = \sum_{n=0}^{\infty} g_{2n}^0(f) Y_{2n}^0(\theta, \phi).$$

Figure 19 plots numerical approximations of these coefficients for a 1-meter length and the frequencies $f_0 = 300 \times \{1, 3, 5, 7\}$ MHz (The lines are added for clarity). The plot shows that the coefficients roll off rapidly with increasing index. Figure 14 plots the first few Legendre coefficients as functions of frequency.

21
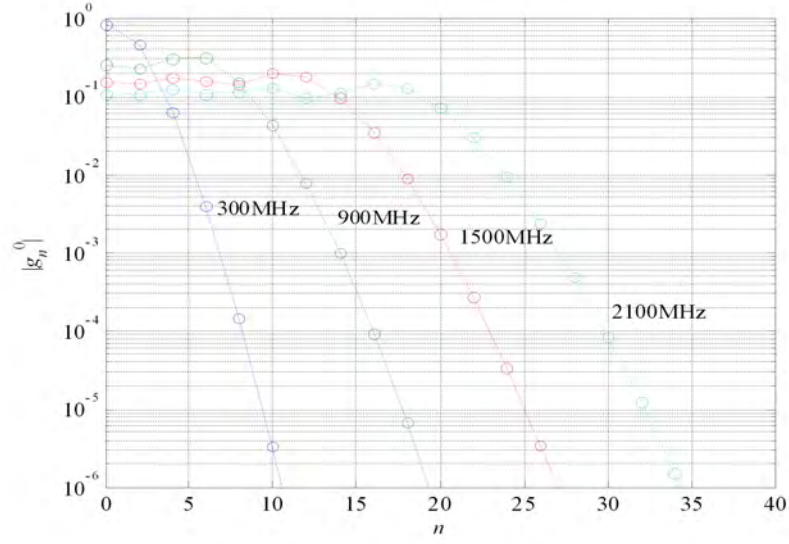
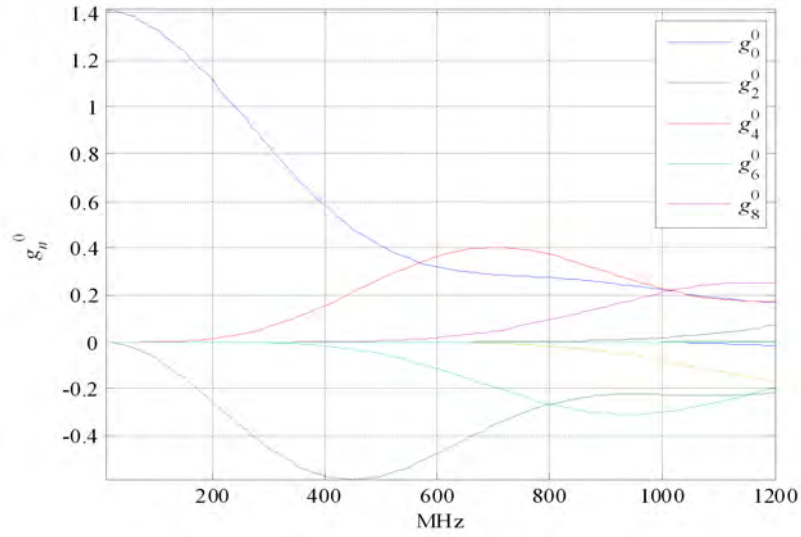Figure 19: Legendre coefficients for selected frequencies.

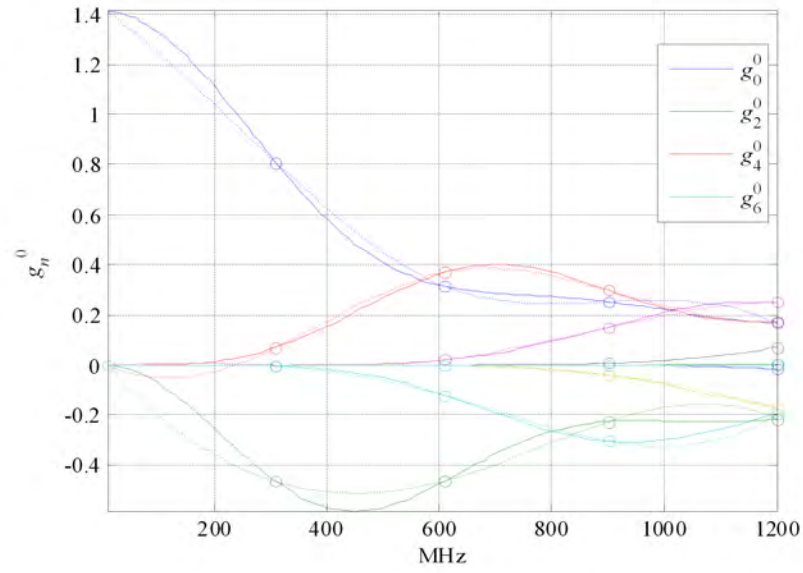Figure 20: Uniform current (selected Legendre coefficients as functions of frequency).

22

Figure 21: Uniform current (Legendre coefficients and five-point splines).
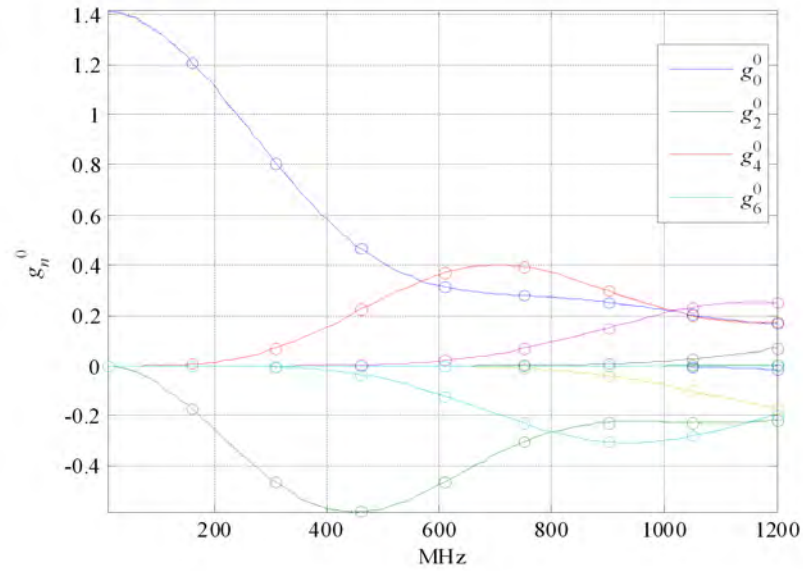

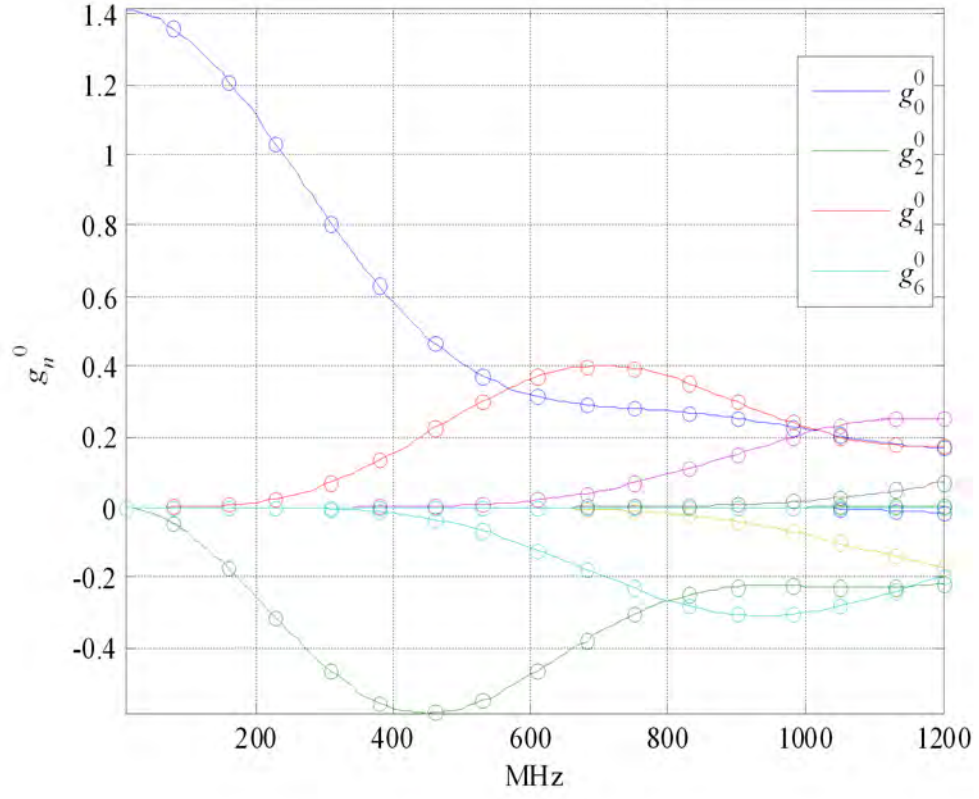Figure 22: Uniform current (Legendre coefficients and 9-point splines).

Figure 23: Uniform current (Legendre coefficients and seven-point splines).

Table 2 reports on the convergence of Algorithm 1. The triple bar is the sup-norm error over all the coefficients:

$$|||g - g_{N_F}|||_\infty := \max\{||g_n^m - g_n^m{}_{N_f}||_\infty : n = 0, 1, \ldots, N; -n \le m \le n\}.$$

This error would not be known to the analyst because the coefficients are not known. This error can be using the "16/15"-rule estimates the error of spline g_{N_F} using the adjacent spline g_{2N_F}. Table 2 reports that this estimate (column 4) is bounding the error in (column 2) For example, the error in spline g_{16} is estimated using g_{32} as the proxy for g:

$$|||g - g_{16}|||_\infty \approx \frac{16}{15}||g_{32} - g_{16}||_\infty = 0.0005352.$$

If the analyst terminates with $N_F = 32$, Algorithm 1 estimates the error in g_{32} the coefficients C_F in column 5:

$$|||g - g_{32}|||_\infty \approx \frac{C_F}{N_F^4} = \frac{33}{32^4} = 0.00003147.$$

Table 2: Spline convergence for the uniform current.

N_F	$|||g - g_{N_F}|||_\infty$	$|||g_{2N_F} - g_{N_F}|||_\infty$	$\frac{16}{15}||g_{2N_F} - g_{N_F}||_\infty$	C_F
4	0.1343	—	0.1440	—
8	0.004521	0.1350	0.004763	33
16	0.0005190	0.004465	0.0005352	17
32	0.00003824	0.0005017	—	30

6 Applications

This section reviews recent applications of spherical harmonic expansions to multi-antenna systems, antenna bounds, and exploiting the sparsity of the spherical pattern expansions with compressed sensing. The spherical harmonics separate the interaction of the antenna and the communication channel and shows that the harmonics can be interpreted as "modes" to connect the transmitter to the receiver [5], CY:2010, [6]. These topics extend the capabilities of antenna performance, design, and wireless propagation at SPAWAR.

6.1 MIMO

This report stated with the applications of the spherical harmonic expansions to indoor wireless using a single transmitter and receiver. Figure 24 is a system diagram of a MIMO radio using two antennas at the transmitter and two antennas at the receiver.

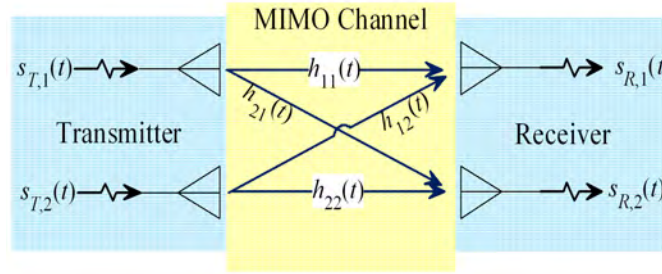Figure 24: 2×2 MIMO system schematic.

The received signal $\mathbf{s}_R(t)$ is modeled as the convolution of the transmitted signal $\mathbf{s}_T(t)$ with the channel matrix:

$$\mathbf{s}_R(t) = \int_{-\infty}^{\infty} H(t - \tau)\mathbf{s}_T(\tau)\,d\tau.$$

The channel matrix

$$H(t) = \sum_{n=1}^{\infty} H_n(t)\delta(t - \tau_n),$$

26

includes all the rays, fading processes, and antenna gains in each random process $\{H_n(t)\}$. Glazunov's 2009 Ph.D thesis made a fundamental application of spherical harmonics to MIMO systems where he shows that [5]:

> ...optimum decorrelation of the antenna signals is obtained by the excitation of orthogonal spherical vector waves modes.

That is, optimal MIMO performance can be computed using these modes [6]:

> ...the expansion of the MIMO channel matrix, H, in spherical vector wave modes of the electromagnetic field of the antennas as well as the propagation channel ... [that] maps the modes excited by the transmitting antenna to the modes exciting the receive antennas and vice versa.

This approach computes MIMO capacity [13]:

> ...the use of spherical harmonics ...decouples the effects of the antennas and the propagation medium. ...[and] illustrate how channel capacity is dependent on the number and distribution of the antennas spherical modes

This approach computes the capacity of a MIMO system that uses polarization as part of the MIMO diversity. Figure 25 is a schematic of a 2×2 MIMO system.
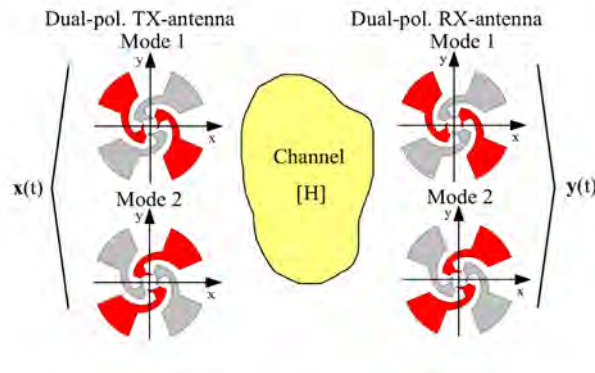

Figure 25: 2×2 dual-mode MIMO [9].

From [9]: "The four-arm antenna structures provide orthogonal-polarized operational modes by feeding one of the two adjacent antenna arm pairs with

27

an odd phase relation." The spherical mode expansion can accurately model the antenna correlations. Because antenna correlation is directly related to the MIMO channel capacity or diversity gain, the spherical-mode expansions provide a modal approach to analyze the MIMO channel.

6.2   Antenna Gain

The classic antenna bounds of Chi have been generalized by Kogan [8]:

> The algorithm of calculation of a high bound of antenna gain occupying area of space, restricted some sphere and operating in given frequency band is given. It is supposed, that the antenna is linear, obeys to a principle of a causality and passivity. The algorithm is based on determination of a extremal gain of an antenna unit radiating a sole spherical harmonic.

Kogan's approach synthesize Chi's circuits with the wideband Fano computations using the spherical harmonics to link a circuit and a mode. This approach may apply to bound the limits of wideband patterns.

6.3   Compressed Sensing and Pattern Interpolation

If a signal is "sparse" in the frequency domain, then sub-Nyquist sampling in the time domain can recover to the signal to arbitrary accuracy. Likewise, for those antenna patterns that have sparse spectral harmonics. the antenna patterns can be recovered from a limited number of samples on the sphere [12].

This compressed sensing result will not reduce the method of moment computations. All the current must be computed before any part of the antenna's pattern can be calculated. However, an application may be found in an inverse problem: recovering and identifying a pattern from a limited number of observations. Consequently, there may be a natural connection between general theory of compressed sensing and the specific radon-transform algorithms of ISAR.

References

[1] Arfken, George [1970] *Mathematical Methods for Physicists*, second edition, Academic Press, New York, NY.

[2] Burghelea, R.; Avrillon, S.; Uguen, B. [2009] UWB antenna compact modeling using vector spherical harmonic theory, *Antennas and Propagation Society International Symposium*, APSURSI '09.

[3] Caratelli, D.; Yarovoy, A. [2010] Unified Time- and Frequency-Domain Approach for Accurate Modeling of Electromagnetic Radiation Processes in Ultrawideband Antennas, *IEEE Transactions on Antennas and Propagation*,58(10), pages 3239–3255.

[4] Corson, Dale R. and Paul Lorrain [1962] *Introduction to Electromagnetic Waves*, W. H. Freemand and Company, San Francisco, CA.

[5] Glazunov, A. [2009] *On the antenna-channel interactions: A spherical vector wave expansion approach*, Ph.D. dissertation, Lund University, 2009.

[6] Glazunov Andrés Alayón, Mats Gustafsson, Andreas F. Molisch, and Fredrik Tufvesson [2009] Physical Modeling of MIMO Antennas and Channels by Means of the Spherical Vector Wave Expansion *Department of Electrical and Information Technology*, Lund University, Sweden.

[7] Harrington, [1961] *Time-Harmonic Electromagnetic Fields*, McGraw-Hill, New York, NY.

[8] Kogan, B. L. [2006] Maximum Accessible Gain of an Antenna, *First European Conference on Antennas and Propagation* EuCAP 2006. , vol., no., pp.1-7, 6-10 Nov. 2006

[9] Klemp, O., G. Armbrecht, and H. Eul [2006] Computation of antenna pattern correlation and MIMO performance by means of surface current distribution and spherical wave theory, *Advances in Radio Science*, 4, pages 33–39.

[10] Jeanne Rockway [2005] *Electromagnetic Field Determination of Antenna Systems in Complex Structural Environments by the Spherical Harmonic Interface Procedure*, PhD Thesis, Ohio State University

[11] Stoer, J. and R. Bulirsch [1980] *Introduction to Numerical Analysis*, Springer-Verlag, New York, NY.

[12] Rauhut, Holger and Rachel Ward [2011] Sparse recovery for spherical harmonic expansions, arXiv:1102.4097v1 [math.NA] 20 Feb 2011.

[13] Ximenes, Leandro R. and André L. F. de Almeida [2010] Capacity Evaluation of MIMO Antenna Systems Using Spherical Harmonics Expansion

1. REPORT DATE *(DD-MM-YYYY)* July 2011	2. REPORT TYPE Final	3. DATES COVERED *(From - To)* May 2011 to July 2011	
4. TITLE AND SUBTITLE INTERPOLATING SPHERICAL HARMONICS FOR COMPUTING ANTENNA PATTERNS		**5a. CONTRACT NUMBER**	
		5b. GRANT NUMBER	
		5c. PROGRAM ELEMENT NUMBER	
6. AUTHORS J. Rockway J. Meloling J. C. Allen		**5d. PROJECT NUMBER**	
		5e. TASK NUMBER	
		5f. WORK UNIT NUMBER	
7. PERFORMING ORGANIZATION NAME(S) AND ADDRESS(ES) SSC Pacific San Diego, CA 92152–5001		**8. PERFORMING ORGANIZATION REPORT NUMBER** TR 1999	
9. SPONSORING/MONITORING AGENCY NAME(S) AND ADDRESS(ES) Air Force Research Laboratory (AFRL) 88 Air Base Wing Public Affiars 5215 Thurlow Street, Bldg. 70 Wright-Patterson Air Force Base, Ohio 45433-5543		**10. SPONSOR/MONITOR'S ACRONYM(S)** A AFRL	
		11. SPONSOR/MONITOR'S REPORT NUMBER(S)	

12. DISTRIBUTION/AVAILABILITY STATEMENT

Approved for public release; distribution is unlimited.

13. SUPPLEMENTARY NOTES

This is the work of the United States Government and therefore is not copyrighted. This work may be copied and disseminated without restriction. Many SSC San Diego public release documents are available in electronic format at http://www.spawar.navy.mil/sti/publications/pubs/index.html

14. ABSTRACT

This report reviews spherical harmonic expansions to compute wideband antenna patterns. Some "antenna" patterns, such as the far-field of a ship, require lots of computer time per each frequency. Consequently, computing such a pattern across a wide frequency band at each frequency is prohibitive. Spherical harmonics offer an alternative—compute the pattern over a coarse sampling across the frequency band, interpolate the spherical harmonics, and use these harmonics to recover the pattern at a fine frequency sampling with small CPU. This report develops an adaptive spline interpolation algorithm with error control. The development used antennas with smooth analytic patterns for verification. Further developments must test this algorithm on a suite of tactical antenna patterns.

15. SUBJECT TERMS

Mission Area: Communications
multiple input multiple output   adaptive spline interpolation   pattern interpolation
spherical harmonics   compressed sponsor

16. SECURITY CLASSIFICATION OF:			17. LIMITATION OF ABSTRACT	18. NUMBER OF PAGES	19a. NAME OF RESPONSIBLE PERSON Jeffrey Allen	
a. REPORT	b. ABSTRACT	c. THIS PAGE				
U	U	U	U	42	**19B. TELEPHONE NUMBER** *(Include area code)* (619) 553–6566	

INITIAL DISTRIBUTION

SSC Pacific
San Diego, CA 92152-5001